THE JOURNAL OF PHYSICAL CHEMISTRY C

Subscriber access provided by Colorado State University | Libraries

C: Energy Conversion and Storage; Energy and Charge Transport

RDX and HMX Related Anionic Species Explored by Photoelectron Spectroscopy and Density Functional Theory

Zhen Zeng, and Elliot R. R. Bernstein

J. Phys. Chem. C, **Just Accepted Manuscript** • DOI: 10.1021/acs.jpcc.8b07728 • Publication Date (Web): 12 Sep 2018

ACS Publications

is published by the American Chemical Society. 1155 Sixteenth Street N.W., Washington, DC 20036

RDX and HMX Related Anionic Species Explored by Photoelectron Spectroscopy and Density Functional Theory

Zhen Zeng, Elliot R. Bernstein*

Department of Chemistry, NSF ERC for Extreme Ultraviolet Science and Technology, Colorado State University, Fort Collins, CO 80523, USA

**E-mail: erb@colostate.edu*

ABSTRACT

Anion photoelectron spectroscopy (PES), supported by Density Functional Theory (DFT) calculations, is employed to study energetic materials RDX (3,5-trinitroperhydro-1,3,5-triazine) and HMX (octahydro-1,3,5,7-tetranitro-1,3,5,7-tetrazocine). Their isolated anions and decomposition products are generated by matrix assisted laser desorption ionization (MALDI). Their anionic parent species are not observed, but instead accessible fragmentation ions are detected. The vertical detachment energies (VDEs) of these anionic, dissociation generated species are experimentally determined, and the corresponding structures are identified by comparing DFT calculated VDEs to the experimental ones. RDX^- and HMX^- can fragmentate through loss of HNO_2, NO_2, and NCH_2 groups. RDX^- loses up to two NO_2 groups and one NCH_2 moiety, and HMX^- can fragment by up to three NO_2 groups and two NCH_2 moieties. The mass units of $(RDX - H - NO_2)^-$, $(RDX - H - (NO_2)_2)^-$, and $(RDX - NCH_2 - (NO_2)_2)^-$ are the same as those of $(HMX - H - (NO_2)_2 - NCH_2)^-$, $(HMX - H - (NO_2)_3 - NCH_2)^-$, and $(HMX - (NO_2)_3 - (NCH_2)_2)^-$, respectively. These dissociation related anions with the same mass units share nearly identical photoelectron spectra and geometrical structures, which suggest structural and dissociation routine similarities between RDX and HMX anions. By way of comparison, energetic material TATB (2,4,6-triamino-1,3,5-trinitrobenzene) has also been considered: its parent anion generated through MALDI processes can be observed in the mass spectrum. The observation of $TATB^-$ parent anion, but not RDX^- and HMX^- parent anions, is consistent with TATB's higher thermal stability than those of RDX and HMX.

I. INTRODUCTION

Nitro-heterocyclic energetic materials RDX (3,5-trinitroperhydro-1,3,5-triazine), and HMX (octahydro-1,3,5,7-tetranitro-1,3,5,7-tetrazocine) are commonly used solid propellants and chemical explosives for both widespread military and commercial purposes. They have similar molecular structures and share chemical similarity. They are classified as nitramines with interacting CH_2 and $N\text{-}NO_2$ moieties, and characterized as cyclohexane and cyclooctane with nitramine groups: presence of nitramine groups is vital to their explosive kinetics. RDX is known to exist in five crystalline polymorphs (α, β, γ, ε, and δ), while HMX has four crystalline phases (α, β, γ, and δ), depending on different temperature and pressure conditions. Phase transitions at high pressure are identified by using vibrational spectroscopy.[1-7]

Combustion mechanisms and decomposition behavior are extremely important for understanding ignition and energy release chemistry of RDX and HMX, especially at different temperature, pressure, or phase conditions. Many experimental investigations have been devoted to the study of thermal decomposition behaviors of RDX and HMX.[8-9] Through in situ, rapid-scan Fourier transform infrared spectroscopy studies, NO_2 is identified as the predominant initial gas product from RDX, and HCN from HMX. CH_2O, N_2O and HONO are also determined to be important initial products of pyrolysis.[10] Thermal degradation of RDX has also been time-resolved and kinetically analyzed over selected thermal ranges with a pyrolysis unit interfaced to an atmospheric pressure chemical ionization tandem mass spectrometry (MS-MS) system.[11] The pyrolysis process and pyrogenic products of RDX and HMX are further identified using pyrolysis-gas chromatography and pyrolysis capillary gas chromatography–mass spectrometry, and it is found that HMX and RDX have similar pyrolysis mechanisms.[12] The thermal kinetic parameters of decompositions of RDX and HMX are determined using thermal analytical techniques (thermogravimetric analysis and differential scanning calorimetry).[13] Some combustion-wave structures are analyzed via a microthermocouple technique by measuring temperature distributions in powder combustion waves.[14] A thermal decomposition study of RDX through molecular dynamics simulations at a variety of temperatures and densities identifies appearance times and equilibrium populations of products CO, CO_2, N_2 and H_2O.[15]

These cyclic nitramine energetic materials can release significant amounts of energy through a complicated bulk decomposition process, involving both

unimolecular, and perhaps even multimolecular, reactions. A molecular level understanding of the underlying complex chemical processes is essential to obtain the critical information for initial chemical steps of decomposition, chemical reaction pathways, as well as molecular structure of intermediates and end products. The total energy release process must involve all RDX and HMX species (i.e., ground and excited electronic state neutrals, as well as positive and negative ions in various degrees of electronic excitation).[16-19]

Different theoretical investigations focusing on possible unimolecular decomposition mechanisms for RDX and HMX suggest that NO_2 fission, HONO elimination, concerted ring breaking, and dissociation of the ring along the C–N bond are some of the neutral molecule ground state decomposition pathways.[20-26] Another initiation decomposition mechanism of HMX and RDX with the unimolecular C–H bond cleavage has also been suggested.[27-30]

The experimental investigations of degradation products and unimolecular decomposition mechanisms include mass spectrometry[31-37] and laser spectroscopy measurements. Mass spectrometry is also widely employed for trace levels of energetic materials detection by in conjunction with many different analytical approaches, including liquid chromatography, gas chromatography, laser-induced ionization, and electrospray ionization, etc.[38-44]

A negative chemical ionization combined with tandem mass spectrometry has been used to identify fragmentation patterns of RDX: such patterns demonstrate pathways for elimination of NO_2 and NO_3, and suggests anion-molecule complexes with axial N-N bond cleavage instead of formation of RDX anion.[44] Laser ionization time of flight mass spectrometry analysis of explosive compounds has been performed on RDX; dependence of resultant spectra on the laser energy or fragmentation pathways is suggested.[45-48] Infrared multiphoton decomposition experiments have been dedicated to illustrate that OH radicals are formed in the unimolecular decomposition of neutral ground state RDX and HMX,[49] and three $CH_2N_2O_2$ fragments can be produced through concerted symmetric triple fission of RDX.[50] $CH_2N_2O_2$ fragments can subsequently undergo secondary concerted dissociation to produce HCN, H_2CO, HONO (or HNO_2), and N_2O.

Fourier transform infrared spectroscopy (FTIR),[51], X-ray photoelectron spectroscopy (XPS), and electron paramagnetic resonance (EPR) spectroscopy[52] have been utilized to study the initial decomposition behavior of EMs due to laser irradiation. Time-resolved optical spectroscopic techniques (emission, absorption,

transmission, and Raman spectroscopies) are used to examine shock wave induced chemical decomposition of RDX: NO_2 radicals are suggested to be generated in the initial decomposition. Nonetheless, bimolecular reactions between unreacted RDX and free radicals are evident on high stress samples.[53-54] A photodecomposition study following 248 nm photolysis of RDX has reported electronically excited NO_2 and OH, which are suggested to derive from N-N bond scission, followed by HONO elimination.[55] More photodissociation studies using laser-induced fluorescence spectroscopy or ultrafast UV femtosecond laser pump-probe techniques find NO as the observed initial decomposition product of RDX and HMX from their neutral excited electronic states: NO_2, HONO, or CH_2NNO_2 are not intermediates for NO under these conditions.[16-17, 56] A laser induced breakdown spectroscopic study of RDX and HMX shows presence of C and CN mass peaks, which are signatures of highly energy materials.[57] Dissociative electron attachment to HMX with an electron energy range of 0–20 eV gives rise to two most intense ions NO_2^- and $C_3H_6N_5O_4^-$.[58] Electron affinity and mass spectral decomposition mechanisms of RDX isomers upon electron attachment have been investigated theoretically: the vertical detachment energies are calculated to be between 1.3 and 4.0 eV with NO_2^- loss common for anions.[59]

From these previous studies, one concludes that RDX/HMX, and for that matter all energetics, release their stored chemical energy through reactions that are dependent on different neutral, ionic, and excited state species at the ultrafast initiation process. Less attention has been focused, however, upon structural characterization of the generated products and intermediates. Thereby, the intrinsic initial unimolecular decomposition mechanisms have not been fully addressed. Gas phase studies of isolated atomic/molecular ions produced through decomposition of energetic materials can be employed to explore the decomposition patterns and structural details, and eventually explicate the full nature of all unimolecular decomposition mechanisms for all generated species.

In the present work, we initiate anion photoelectron spectroscopy (PES) studies jointly with density functional theory (DFT) analysis for the nitramines RDX and HMX (Figure. 1) and their related decomposition anionic species. Their electronic and geometric structures are fully identified and characterized. The experimental observations (vertical detachment energy, VDEs), coupled with theoretical calculations of structures and VDEs, give insights into initial decomposition intermediates/products arising from one or multiple bond cleavages and structural and electronic rearrangement, further highlighting their reactive and highly

energetic nature. One very clear and obvious conclusion from these prior studies in our laboratory[16-18, 56, 60] is that release of stored chemical energy from energetic molecules depends on the generation of excited vibronic states of neutral molecules, and the generation of both anions and cations of the energetic molecules and their fragmentation species.

TATB (2,4,6-triamino-1,3,5- trinitrobenzene), with three nitro groups (NO_2) and three amine (NH_2) groups attached to an aromatic carbon ring, is additionally an important explosive that is insensitive to shock, vibration, fire, or impact, and that is also widely employed for military and civilian application.[61] Thermal decomposition studies based on spectroscopic and thermal analysis techniques suggest that C-NH_2 bond rupture appears to be the primary step in the thermolysis of TATB, and NH_3, CO_2, NO_2, HCN, and H_2O are produced in its initial stages of decomposition.[62] Photoinduced decomposition of TATB is investigated via ultrafast time-resolved infrared and steady-state Fourier transform IR spectroscopies: decomposition products vary with pressure and CO_2 is a decomposition product at ambient pressure and H_2O is a decomposition product at elevated pressure.[63] Theoretical investigations of initial decomposition mechanisms of TATB find that decomposition pathways include N−H, N−O, C−NH_2 bond dissociation, C-NO_2 bond cleavage, N_2 formation, NO_2–ONO isomerization within different electronic states, and ring closures mediated by intramolecular hydrogen transfer.[64-67] Some efforts have been dedicated to combining TATB with other energetics and with polymers to generate new and specific formulations. Their properties, behaviors, and performances have subsequently been analyzed.[68-72] Employing the same techniques used for RDX and HMX, the TATB parent anionic species is observed, unlike the case for RDX and HMX, further demonstrating its higher overall stability.

II. EXPERIMENTAL PROCEDURES

The experimental apparatus consists of three parts: a pulsed supersonic nozzle with an attached matrix assisted laser desorption ionization (MALDI) source, a reflectron time of flight mass spectrometer (RTOFMS), and a magnetic bottle photoelectron TOF spectrometer (MBTOFPES). Details of this system (RTOFMS/MBTOFPES) can be found in our previous publications.[16, 73] The nozzle employed for the sample beam generation is constructed from a Jordan Co. pulsed valve with a home made laser desorption attachment. Sample drums for the

MALDI process are prepared by wrapping the sample desorption substrate Zn on a clean Al drum.[18] A mixed solution of EM sample and matrix (R6G or DCM) dye with mole ratio 1:2 in a solvent (typically, methanol or acetonitrile) is uniformly sprayed on the drum/substrate surface using an air atomizing spray nozzle (Spraying System Co.) with siphon pressure of 10 psig. During the spraying process, the sample drum is rotated under heat of a halogen lamp in a fume hood to ensure deposition of EM and matrix on the drum surface is homogeneous and dry. The well coated and dried sample drum is then placed in the laser ablation head/nozzle assembly and put into the vacuum chamber. Second harmonic (532 nm) light pulses from a Nd:YAG laser are used to ablate the sample drum, which rotates and translates simultaneously to maintain a fresh sample area for each laser ablation pulse. Intact EM molecules are desorbed from the drum, interact with other species (including electrons) in the ablated material, and are entrained in the supersonic flow of helium carrier gas with a 50 psi backing pressure through a 2 × 60 mm channel in the ablation head, and expanded into the sample chamber.

With a closed pulsed valve, the RTOFMS chamber pressure is ~ 6×10^{-8} Torr. Generated molecular anions are pulsed into the RTOFMS and are mass analyzed using the RTOFMS. For PES experiments, specific anions are first mass selected and decelerated before interacting with a 532 nm (2.331 eV), 355 nm (3.496 eV), or 266 nm (4.661 eV) laser beam from another Nd:YAG laser in the photodetachment region. Photodetached electrons are collected and energy analyzed by the MBTOFPES at nearly 100% efficiency. The photodetachment laser is operated at a 10 Hz repetition rate, while the ablation laser is synchronously triggered at 5 Hz. Data are collected at 5 Hz employing a background subtraction with alternation of the ablation laser on/off when the detachment laser generates 266 nm or higher energy photons. Every photoelectron spectrum is calibrated by the known spectra of Cu^- and Pb^- at the employed detachment photon energy. The photoelectron energy resolution is ~ 4% (40 meV for 1 eV kinetic energy electrons), as anticipated for a 1 m PES flight tube.

III COMPUTATIONAL METHODS

In the present work, all calculations are implemented in the Gaussian 09 program[74] using density function theory (DFT) employing the B3LYP[75-77] functional and 6-311++G(d,p) basis set for all atoms. B3LYP/6-311++G(d,p) level of theory has been evaluated for accurate prediction of properties of energetic materials in

previous EMs studies.[19, 60] Geometry optimization is conducted by manually creating initial structures at every possible arrangement. No symmetry restrictions are applied for the calculations. Optimization of the low lying isomers for each anion is performed with harmonic vibrational frequencies calculated to confirm that the obtained structures are the true local minima. Theoretical VDEs for each anionic species are calculated as the energy difference between the ground state of the anion and its corresponding neutral at the same structure as the anion. For further electronic structure based understanding of energetic materials related species behavior, a Natural Bond Orbital (NBO, as implemented in the Gaussian 09 program suite) analysis is performed based on the B3LYP/6-311++G(d,p) level of theory.

IV. EXPERIMENTAL RESULTS

Mass spectra of RDX and HMX, generated through the MALDI process, are displayed in Figures 2 and 3, respectively. (See Supporting Information about the discussion of contamination possibility of RDX and HMX samples) No parent anionic species are observed in the mass spectra; additional associated decomposition anions $(RDX - H - NO_2)^-$, $(RDX - H - (NO_2)_2)^-$, $(RDX - NCH_2 - (NO_2)_2)^-$, $(HMX - NO_2)^-$, $(HMX - H - (NO_2)_2)^-$, $(HMX - H - (NO_2)_2 - NCH_2)^-$, $(HMX - H - (NO_2)_3 - NCH_2)^-$, and $(HMX - (NO_2)_3 - (NCH_2)_2)^-$, respectively, are instead accessible. A small fragmentation anion NO_2^- is also assigned. Their corresponding photoelectron spectra are recoded via 266 nm photons; VDEs are measured from the maxima of the corresponding PES peaks. As shown in Figure 4, the photoelectron spectrum of $(RDX - H - NO_2)^-$ shows a high electron binding feature centered above 4.4 eV, with a broad, considerably weaker peak at lower binding energy in the range ~1 eV to ~3.5 eV. The PES of $(RDX - H - (NO_2)_2)^-$ evidences two features (Figure 5), centered at 2.97 and 4.15 eV, respectively. $(RDX - NCH_2 - (NO_2)_2)^-$ has a single narrow PES peak centered at 4.10 eV (see Figure 6). In Figure 7, a broad feature centered at around 2.84 can be observed for $(HMX - NO_2)^-$. The photoelectron spectrum of $(HMX - H - (NO_2)_2)^-$ exhibits a broad peak with maximum position higher than 3.5 eV (Figure 8). For $(HMX - H - (NO_2)_2 - NCH_2)^-$, its PES (Figure 9) shows a peak centered at 3.99 eV, and higher EBE tail exceeding 266 nm photon energy. A shoulder at lower EBE also appears. $(HMX - H - (NO_2)_3 - NCH_2)^-$, evidences two major PES features (2.97 and 4.20 eV), identical to that of $(RDX - H - (NO_2)_2)^-$, but with different relative

intensities, as can be seen from Figure 10. In Figure 11, a narrow feature centered at 4.17 eV is accessible for $(HMX - (NO_2)_3 - (NCH_2)_2)^-$, similar to the PES peak of $(RDX - NCH_2 - (NO_2)_2)^-$.

TATB parent anion is observed in the mass spectrum. Its photoelectron spectrum is presented in Figure 12. The weak peak is centered at ~2.05 eV. The intensity of fragmentation ions $(TATB\text{-}NH_2)^-$ is too weak to be detected in the PES system.

The experimental VDEs of $(RDX - H - NO_2)^-$, $(RDX - H - (NO_2)_2)^-$, $(RDX - NCH_2 - (NO_2)_2)^-$, $(HMX - NO_2)^-$, $(HMX - H - (NO_2)_2)^-$, $(HMX - H - (NO_2)_2 - NCH_2)^-$, $(HMX - H - (NO_2)_3 - NCH_2)^-$, and $(HMX - (NO_2)_3 - (NCH_2)_2)^-$ are summarized in Table 1.

V. THEORETICAL RESULTS

The low-lying isomers of RDX and HMX related anionic species, and TATB parent anion, are summarized in Figures 12 to 16. Their calculated VDEs and relative energies are summarized in Table 1 and compared with the experimentally determined values.

a) RDX

Two low lying isomers of RDX^- parent anion are calculated and shown in Figure 13. The lowest energy isomer RDX^- (A) has a structure with one NO_2 group weakly interacting with the ring backbone (longer axial N-N distance of 2.35 Å compared to other two N-N bond lengths of 1.36 Å). The less stable isomer RDX^- (B) has a relative energy of 0.51 eV with respect to that of the most stable isomer. Its structure appears with N-N bond lengths of 1.41 Å. Their calculated VDEs are 4.38 and 1.77 eV, respectively.

For $(RDX - H - NO_2)^-$, two low lying isomers are exhibited in Figure 14 (I). The lowest energy isomer $(RDX - H - NO_2)^-$ (A) has a structure similar to that of the most stable parent anionic structure RDX^- (A) with one of the remaining NO_2 groups weakly bond (axial N-N distance: 2.41 Å). Its theoretical VDE is calculated to be 4.51 eV, in good agreement with the experimental determination (> 4.4 eV). Isomer $(RDX - H - NO_2)^-$ (B) has both NO_2 groups residing on the ring structure. The calculated VDE of $(RDX - H - NO_2)^-$ (B) is 2.97 eV, in the range of a broad shoulder of the experimental PES. Thus, the photoelectron spectrum of (RDX – H

– $NO_2)^-$ is mainly contributed by isomer $(RDX – H – NO_2)^-$ (A) with the presence of $(RDX – H – NO_2)^-$ (B) is also possible.

Two low lying isomers for $(RDX – H – (NO_2)_2)^-$ are exhibited in Figure 14 (II). The most stable isomer $(RDX – H – (NO_2)_2)^-$ (A) has an open ring structure with C-N bond fission. The calculated VDE of $(RDX – H – (NO_2)_2)^-$ (A) is 4.27 eV, consistent with the higher VDE peak (4.15 eV) from the experimental PES. Isomer $(RDX – H – (NO_2)_2)^-$ (B) has an intact ring structure with a relative energy of 0.21 eV with respect to that of isomer (A). The theoretical VDE of $(RDX – H – (NO_2)_2)^-$ (B) is 2.97 eV, in excellent agreement with the experimental feature at the lower EBE portion of the spectrum. Thereby, the two PES features for $(RDX – H – (NO_2)_2)^-$ are contributed by two distinct isomers: one with a ring open structure and one with a closed ring structure.

$(RDX – NCH_2 – (NO_2)_2)^-$ shows two similar structures with nearly degenerate energies. Through losing an NCH_2 group, the ring open N-C-N-C back bones in the two isomers have slightly different arrangements. Their calculated VDEs are 3.94 and 3.95 eV, close to the experimental determination (4.10 eV).

b) HMX

In Figure 13, the HMX^- parent anion displays a lowest energy geometry with one elongated axial N-N distance inducing one NO_2 group to be only weakly bound to the ring. This situation and structure are identical to that found for the RDX^- parent anion. HMX^- has a calculated VDE of 2.21 eV.

For the $(HMX – NO_2)^-$ anion, two optimized low lying isomers are displayed in Figure 15 (I). The most stable isomer $(HMX – NO_2)^-$ (A) shows ring cleavage with C-N bond scission. Its theoretical VDE is calculated to be 4.99 eV, higher than the 266 nm photo energy. Isomer $(HMX – NO_2)^-$ (B) has semi ring shape but with two elongated C-N bonds (1.57 Å) than averaged C-N bonds (1.44 Å). It has a calculated VDE of 3.93 eV, in reasonable consistence with the broad PES tail at higher EBE part (> 3.5 eV). Thus, isomer (B) can be assigned to be present in the experiments. A major PES feature centered at 2.84 eV has not as yet been identified through calculations: this feature could be associated with the presence of some unknown contamination in the HMX sample.

For $(HMX – H – (NO_2)_2)^-$, as shown in Figure 15 (II), the lowest energy isomer (A) has obvious ring cleavage geometry through N-C bond breaking. Its calculated VDE is 4.93 eV, exceeding the 266 nm photon energy. Isomer (HMX – H –

$(NO_2)_2)^-$ (B) has weaker ring C-N interaction and a deformed ring conformation compared to that of the parent species. It has a calculated VDE of 3.90 eV, in reasonable agreement to the experimental determination (> 3.5 eV). Thus, the 266 nm PES is mainly contributed by isomer (B).

As can be seen from Figure 16 (I), the two low lying isomers of (HMX – H – $(NO_2)_2$ – $NCH_2)^-$ display different structures. Isomer (HMX – H – $(NO_2)_2$ – $NCH_2)^-$ (A) has an intact six-member ring evidencing one NO_2 group bound tightly to the ring (axial N-N bond length of 1.34 Å) and another NO_2 group interacting weakly (axial N-N bond distance of 2.54 Å). The calculated VDE is 4.22 eV, in agreement with the experimental observation of 3.99 eV. Isomer (HMX – H – $(NO_2)_2$ – $NCH_2)^-$ (B) has no apparent ring structure, but has an NCH moiety interacting with an NO_2 group through hydrogen bonding. The theoretical VDE is 4.34 eV, in the range of the higher EBE tail of the PES spectrum of (HMX – H – $(NO_2)_2$ – $NCH_2)^-$. Thereby, (HMX – H – $(NO_2)_2$ – $NCH_2)^-$ can exist as both isomers (A) and (B).

For (HMX – H – $(NO_2)_3$ – $NCH_2)^-$ (Figure 16 (II)), the most stable isomer (A) exhibits an open ring structure through a C-N bond rupture, while isomer (B) still has an intact six-member ring with a relative energy of 0.21 eV with regard to that of (A). Their theoretical VDEs are calculated to be 4.27 and 2.98 eV, respectively, consistent with the two observed experimental VDEs (4.20 and 2.97 eV). They are both present in the experiments and contribute to the two PES features of (HMX – H – $(NO_2)_3$ – $NCH_2)^-$, respectively.

The two low lying isomers (A) and (B) of (HMX – $(NO_2)_3$ – $(NCH_2)_2)^-$ are nearly degenerated in energy, and are depicted in Figure 16 (III). They have slightly different structures for the linear C-N-C bond arrangements. Their calculated VDEs (3.81 and 3.82 eV) are close to the experimental VDE of 4.17 eV. Thus, both isomers (HMX – $(NO_2)_3$ – $(NCH_2)_2)^-$ (A) and (B) are probably observed in our experiments.

c) TATB

The optimized anionic structure of $TATB^-$ and its calculated VDE (2.34 eV) are shown in Figure 12. The structure shows ring conformation and tightly bound NO_2 groups (C-N bond lengths: 1.34 and 1.42Å). The theoretical VDE (2.34 eV) is consistent with the experimental VDE of 2.05 eV, further confirming the anionic structure present in the gas phase and the accurate VDE prediction based on B3LYP/6-311++G(d,p) level of theory.

VI DISCUSSION

Parent anionic species RDX^- and HMX^- are not observed in these MALDI experiments, while $TATB^-$ parent anion is. The lowest energy isomers of anionic structures RDX^- and HMX^- are shown to have one NO_2 group weakly bound (elongated axial N-N bonds), while $TATB^-$ parent anion has NO_2 and NH_2 groups all tightly bound to the C-ring backbone. Therefore, RDX^- and HMX^- anions are more likely to undergo dissociation through loss of NO_2/NO_2H group than TATB, which can explain why RDX^- and HMX^- are not observed in our experiments. Additional NBO analysis is performed in order to understand the parent anionic species behavior from the view point of electronic structure: the highest singly occupied molecular orbitals (HSOMO) of the three anionic parent species are presented in Figure 17. The NBO/HSOMOs of RDX^- (A) and HMX^- (A) show main electron distribution on a p orbital component of an N atom forming a σ^* bond, but with only a weak interaction to an NO_2 group. $TATB^-$ displays a major electron distribution on one of the NO_2 group. These electron distributions further suggest the relatively lower stability of RDX^- and HMX^- with regard to dissociation of an NO_2 group than found for $TATB^-$. These comparisons also suggest that, since the anions are a component of the overall energy release mechanisms for RDX, HMX, and TATB, TATB should be more stable with regard to accidental ignition than either of the two nitramines.

RDX^- and HMX^- can both dissociate through loss of HNO_2, NO_2, NCH_2 groups. RDX^- evidences losing up to two NO_2 groups and one NCH_2 moiety, and HMX^- can fragment losing up to three NO_2 groups and two NCH_2 moieties, as shown in Figure 18. Note that $(RDX - H - NO_2)^-$ and $(HMX - H - (NO_2)_2 - NCH_2)^-$ have the same mass. They share similar major PES features with high EBE that can be assigned to nearly identical structures (isomer $(RDX - H - NO_2)^-$ (A) and isomer $(HMX - H - (NO_2)_2 - NCH_2)^-$ (A)) with only a small orientation difference of a weakly bound NO_2 group. Similarly, $(RDX - H - (NO_2)_2)^-$ and $(HMX - H - (NO_2)_3 - NCH_2)^-$ have the same mass and their corresponding two PES peaks have nearly the same positions, which can be contributed by two distinct isomers. These two observed isomers of $(RDX - H - (NO_2)_2)^-$ are nearly identical to those of $(HMX - H - (NO_2)_3 - NCH_2)^-$. $(RDX - NCH_2 - (NO_2)_2)^-$ and $(HMX - (NO_2)_3 - (NCH_2)_2)^-$ also have the same mass and similar PES features with similar isomers

present. These similarities between fragment ions of RDX^- and HMX^- illustrates that HMX^- and RDX should undergo similar dissociation reaction pathways.

VII CONCLUSIONS

Nitramine highly energetic molecules, RDX and HMX, are generated through the MALDI method and their negative ions are subsequently characterized employing anion photoelectron spectroscopic experiments. The PES data are analyzed through DFT calculations of their anion structures and VDEs. The isolated dissociation anions $(RDX - H - NO_2)^-$, $(RDX - H - (NO_2)_2)^-$, $(RDX - NCH_2 - (NO_2)_2)^-$, $(HMX - NO_2)^-$, $(HMX - H - (NO_2)_2)^-$, $(HMX - H - (NO_2)_2 - NCH_2)^-$, $(HMX - H - (NO_2)_3 - NCH_2)^-$, and $(HMX - (NO_2)_3 - (NCH_2)_2)^-$ are observed through RTOFMS and their corresponding photoelectron spectra are recorded. Their VDEs are experimentally determined. Based on the excellent agreements between experimental VDEs and theoretical VDEs, the anionic structures are definitively assigned.

The parent anions RDX^- and HMX^- are not detected in the TOFMS or PES spectra. Their electron binding energies and anionic structures can be assigned based on the tested, accurate calculational algorithm. Both RDX^- and HMX^- parent anions have their lowest energy structures with one NO_2 group weakly bound. This further explains why parent anions are not accessible in RTOFMS: parent anions can dissociate easily by losing NO_2/HNO_2 followed by secondary dissociations and fragmentations. The anionic electronic structures of RDX and HMX have a significant and important effect on their decomposition reactions mechanisms; the missing parent anions further emphasize the active nature of negatively charged RDX and HMX. These anions can decompose readily and rapidly, as has been previously determined for the neutral, electronically excited and other anionic EM molecules.

Anions $(RDX - H - NO_2)^-$, $(RDX - H - (NO_2)_2)^-$, and $(RDX - NCH_2 - (NO_2)_2)^-$ are the characteristic dissociated fragments of RDX upon capturing an extra electron. $(RDX - H - NO_2)^-$ mainly exhibits a ring structure with one NO_2 group weakly bound. Both open and closed ring structures are assigned to contribute to the experimental photoelectron spectra for $(RDX - H - (NO_2)_2)^-$. $(RDX - NCH_2 - (NO_2)_2)^-$ shows open ring structures with one NO_2 group. The structural change gives insight into the dissociation, energy release process for RDX: RDX anion can lose an HNO_2 group first, followed by losing another NO_2 group and an NCH_2

moiety. Fragmentation anion $(RDX - H - NO_2)^-$ is observed from the RTOFMS/PES but not $(RDX - NO_2)^-$. This observation suggests that $(RDX - H - NO_2)^-$ is more energetically favorable than $(RDX - NO_2)^-$ during the fragmentation process.

Anions $(HMX - NO_2)^-$, $(HMX - H - (NO_2)_2)^-$, $(HMX - H - (NO_2)_2 - NCH_2)^-$, $(HMX - H - (NO_2)_3 - NCH_2)^-$, and $(HMX - (NO_2)_3 - (NCH_2)_2)^-$ are identified as the dissociation pattern of HMX with an extra electron. Only open ring structures are identified to contribute to the PES spectrum of $(HMX - H - (NO_2)_2)^-$. $(HMX - H - (NO_2)_2 - NCH_2)^-$, $(HMX - H - (NO_2)_3 - NCH_2)^-$, and $(HMX - (NO_2)_3 - (NCH_2)_2)^-$ show nearly the same structure as comparable anions for RDX related anionic species. These structural similarities indicate that HMX can access the same decomposition structures as does RDX during dissociation processes: the decomposition scheme for HMX is similar to that of RDX.

The mass units of $(RDX - H - NO_2)^-$, $(RDX - H - (NO_2)_2)^-$, and $(RDX - NCH_2 - (NO_2)_2)^-$ are the same as those of $(HMX - H - (NO_2)_2 - NCH_2)^-$, $(HMX - H - (NO_2)_3 - NCH_2)^-$, and $(HMX - (NO_2)_3 - (NCH_2)_2)^-$, respectively. These dissociation anions with the same masses share nearly identical photoelectron spectra and geometrical structures. These explicit results emphasize the structural and dissociation mechanism similarities between RDX and HMX anions. NO_2 and NCH_2 moieties are the major loss units from the respective anions.

The significant instability of RDX and HMX with an excess electron, as well as identification of their dissociation ions, further reinforces their highly reactive and explosive nature. All of these species can release their stored energy through anion and subsequent dissociation anions. Both these anionic and neutral excited states species can be highly involved in the release of stored energy from RDX and HMX molecules and from energetics in general.

The TATB parent anionic species is observed in our RTOFMS/PES system. This difference from the situation for RDX and HMX, further demonstrates TATB's higher thermal stability than that of RDX and HMX.

Supplementary Material

See supplementary material for the discussion of contamination possibility of RDX and HMX samples.

Conflicts of interest

There are no conflicts of interest to declare.

ACKNOWLEDGMENTS

This work is supported by a grant from the US Air Force Office of Scientific Research (AFOSR) through grant number FA9550-10-1-0454, the National Science Foundation (NSF) ERC for Extreme Ultraviolet Science and Technology under NSF Award No. 0310717, the Army Research Office (ARO, Grant Nos. FA9550-10-1-0454 and W911-NF13-10192), and a DoD DURIP grant (W911NF-13-1-0192).

References

(1) Miller, P. J.; Block, S.; Piermarini, G. J. Effects of pressure on the thermal decomposition kinetics, chemical reactivity and phase behavior of RDX. *Combusti. Flame* **1991,** *83*, 174-184.

(2) Dreger, Z. A.; Gupta, Y. M. High pressure Raman spectroscopy of single crystals of hexahydro-1,3,5-trinitro-1,3,5-triazine (RDX). *J. Phys. Chem. B* **2007,** *111*, 3893-3903.

(3) Dreger, Z. A. Energetic materials under high pressures and temperatures: stability, polymorphism and decomposition of RDX. *J. Phys. Conf. Ser.* **2012,** *377*, 012047.

(4) Ciezak, J. A.; Jenkins, T. A.; Liu, Z.; Hemley, R. J. High-pressure vibrational spectroscopy of energetic materials: hexahydro-1,3,5-trinitro-1,3,5-triazine. *J. Phys. Chem. B* **2007,** *111*, 59-63.

(5) Yoo, C.-S.; Cynn, H. Equation of state, phase transition, decomposition of β-HMX (octahydro-1,3,5,7-tetranitro-1,3,5,7-tetrazocine) at high pressures. *J. Chem. Phys.* **1999,** *111*, 10229-10235.

(6) Zeng, Y.; Song, Y.; Yu, G.; Zheng, X.; Guo, W.; Zhao, J.; Yang, Y. A comparative study of 1,3,5-Trinitroperhydro-1,3,5-triazine (RDX) and Octahydro-1,3,5,7-tetranitro-1,3,5,7-tetrazocine (HMX) under high pressures using Raman spectroscopy and DFT calculations. *J. Mol. Struct* **2016,** *1119*, 240-249.

(7) Pravica, M.; Galley, M.; Kim, E.; Weck, P.; Liu, Z. A far- and mid-infrared study of HMX (octahydro-1,3,5,7-tetranitro-1,3,5,7-tetrazocine) under high pressure. *Chem. Phys. Lett.* **2010,** *500*, 28-34.

(8) Bulusu, S.; Weinstein, D. I.; Autera, J. R.; Velicky, R. W. Deuterium kinetic isotope effect in the thermal-decomposition of 1,3,5-trinitro-1,3,5-triazacyclohexane and 1,3,5,7-tetranitro-1,3,5,7-tetraazacyclooctane - its use as an experimental probe for their shock-induced chemistry. *J. Phys. Chem.* **1986,** *90*, 4121-4126.

(9) Oxley, J. C.; Koob, A. B.; Szekeres, R.; Zheng, W. Mechanisms of nitramine thermolysis. *J. Phys. Chem.* **1994,** *98*, 7004-7008.

(10) Oyumi, Y.; Brill, T. B. Thermal decomposition of energetic materials 3. A high-rate, in situ, FTIR study of the thermolysis of RDX and HMX with pressure and heating rate as variables. *Combusti. Flame* **1985,** *62*, 213-224.

(11) Liebman, S. A.; Snyder, A. P.; Kremer, J. H.; Reutter, D. J.; Schroeder, M. A.; Fifer, R. A. Time-resolved analytical pyrolysis studies of nitramine decomposition with a triple quadrupole mass spectrometer system. *J. Anal. Appl. Pyrolysis* **1987,** *12*, 83-95.

(12) Huwei, L.; Rionong, F. Investigation of thermal decomposition of HMX and RDX by pyrolysis-gas chromatography. *Thermochim. Acta* **1989,** *138*, 167-171.

(13) Lee, J.-S.; Hsu, C.-K.; Chang, C.-L. A study on the thermal decomposition behaviors of PETN, RDX, HNS and HMX. *Thermochim. Acta* **2002,** *392-393*, 173-176.

(14) Zenin, A. A.; Finjakov, S. V. Studying RDX and HMX combustion mechanisms by various experimental techniques. *Combust. Explos. Shock Waves* **2009,** *45*, 559-578.

(15) Strachan, A.; Kober, E. M.; Duin, A. C. T. v.; Oxgaard, J.; III, W. A. G. Thermal decomposition of RDX from reactive molecular dynamics. *J. Chem. Phys.* **2005,** *122*, 054502.

(16) Im, H.-S.; Bernstein, E. R. On the initial steps in the decomposition of energetic materials from excited electronic states. *J. Chem. Phys.* **2000,** *113*, 7911-7918.

(17) Greenfield, M.; Guo, Y. Q.; Bernstein, E. R. Ultrafast photodissociation dynamics of HMX and RDX from their excited electronic states via femtosecond laser pump–probe techniques. *Chem. Phys. Lett.* **2006,** *430*, 277-281.

(18) Yuan, B.; Yu, Z.; Bernstein, E. R. Initial mechanisms for the decomposition of electronically excited energetic materials: 1,5′-BT, 5,5′-BT, and AzTT. *J. Chem. Phys.* **2015,** *142*, 124315.

(19) Zeng, Z.; Bernstein, E. R. Photoelectron spectroscopy and density functional theory studies of N-rich energetic materials. *J. Chem. Phys.* **2016,** *145*, 164302.

(20) Chakraborty, D.; Muller, R. P.; Dasgupta, S.; Goddard, W. A. Mechanism for unimolecular decomposition of HMX (1,3,5,7-Tetranitro-1,3,5,7-tetrazocine), an ab initio study. *J. Phys. Chem. A* **2001,** *105*, 1302-1314.

(21) Chakraborty, D.; Muller, R. P.; Dasgupta, S.; Goddard, W. A. The mechanism for unimolecular decomposition of RDX (1,3,5-Trinitro-1,3,5-triazine), an ab initio study. *J. Phys. Chem. A* **2000,** *104*, 2261-2272.
(22) Liu, L.-l.; Liu, P.-j.; Hu, S.-q.; He, G.-q. Ab initio calculations of the N-N bond dissociation for the gas-phase RDX and HMX. *Sci. Rep.* **2017,** *7*, 40630.
(23) Schweigert, I. V. Ab initio molecular dynamics of high-temperature unimolecular dissociation of gas-phase RDX and its dissociation products. *J. Phys. Chem. A* **2015,** *119*, 2747-2759.
(24) Wu, C. J.; Fried, L. E. Ab initio study of RDX decomposition mechanisms. *J. Phys. Chem. A* **1997,** *101*, 8675-8679.
(25) Patidar, L.; Khichar, M.; Thynell, S. T. Identification of initial decomposition reactions in liquid-phase HMX using quantum mechanics calculations. *Combusti. Flame* **2018,** *188*, 170-179.
(26) Molt, R. W.; Watson, T.; Bazante, A. P.; Bartlett, R. J.; Richards, N. G. J. Gas phase RDX decomposition pathways using coupled cluster theory. *Phys. Chem. Chem. Phys.* **2016,** *18*, 26069-26077.
(27) Ge, N.-N.; Wei, Y.-K.; Ji, G.-F.; Chen, X.-R.; Zhao, F.; Wei, D.-Q. Initial decomposition of the condensed-phase β-HMX under shock waves: molecular dynamics simulations. *J. Phys. Chem. B* **2012,** *116*, 13696-13704.
(28) Wu, Q.; Xiong, G.; Zhu, W.; Xiao, H. How does low temperature coupled with different pressures affect initiation mechanisms and subsequent decompositions in nitramine explosive HMX? *Phys. Chem. Chem. Phys.* **2015,** *17*, 22823-22831.
(29) Strachan, A.; van Duin, A. C. T.; Chakraborty, D.; Dasgupta, S.; Goddard, W. A. Shock waves in high-energy materials: the initial chemical events in nitramine RDX. *Phys. Rev. Lett.* **2003,** *91*, 098301.
(30) Ge, N.-N.; Wei, Y.-K.; Song, Z.-F.; Chen, X.-R.; Ji, G.-F.; Zhao, F.; Wei, D.-Q. Anisotropic responses and initial decomposition of condensed-phase β-HMX under shock loadings via molecular dynamics simulations in conjunction with multiscale shock technique. *J. Phys. Chem. B* **2014,** *118*, 8691-8699.
(31) Milton, F. Mass spectrometric investigations of the thermal decomposition of 1,3,5,7-tetranitro-1,3,5,7-tetraazacylooctane (HMX) and 1,3,5-trinitro-1,3,5-triazacyclohexane (RDX). *Mass Spectrom. Rev.* **1992,** *11*, 137-152.
(32) Kozole, J.; Levine, L. A.; Tomlinson-Phillips, J.; Stairs, J. R. Gas phase ion chemistry of an ion mobility spectrometry based explosive trace detector elucidated by tandem mass spectrometry. *Talanta* **2015,** *140*, 10-19.
(33) Suryanarayana, B.; T., A.; A., M. G. W. Electron-impact fragmentation of some secondary aliphatic nitramines. Migration of the nitro group in heterocyclic nitramines. *Org. Mass Spectrom.* **1970,** *3*, 13-21.
(34) Stals, J. Chemistry of aliphatic unconjugated nitramines. Part 7.-Interrelations between the thermal, photochemical and mass spectral fragmentation of RDX. *Transactions of the Faraday Society* **1971,** *67*, 1768-1775.
(35) Maharrey, S.; Behrens, R. Thermal decomposition of energetic materials. 5. Reaction processes of 1,3,5-trinitrohexahydro-s-triazine below its melting point. *J. Phys. Chem. A* **2005,** *109*, 11236-11249.
(36) Florián, J.; Gao, L.; Zhukhovskyy, V.; MacMillan, D. K.; Chiarelli, M. P. Nitramine anion fragmentation: a mass spectrometric and ab initio study. *J. Am. Soc. Mass. Spectrom.* **2007,** *18*, 835-841.
(37) Lei, Z.; Nicholas, P.; Snehaunshu, C.; R., Z. M. T-Jump/time-of-flight mass spectrometry for time-resolved analysis of energetic materials. *Rapid Commun. Mass Spectrom.* **2009,** *23*, 194-202.
(38) Kozole, J.; Tomlinson-Phillips, J.; Stairs, J. R.; Harper, J. D.; Lukow, S. R.; Lareau, R. T.; Boudries, H.; Lai, H.; Brauer, C. S. Characterizing the gas phase ion chemistry of an ion trap mobility spectrometry based explosive trace detector using a tandem mass spectrometer. *Talanta* **2012,** *99*, 799-810.
(39) Mullen, C.; Irwin, A.; Pond, B. V.; Huestis, D. L.; Coggiola, M. J.; Oser, H. Detection of explosives and explosives-related compounds by single photon laser ionization time-of-flight mass spectrometry. *Anal. Chem.* **2006,** *78*, 3807-3814.

(40) J., B. J.; J., J. E.; J., L. R. Identification of explosives and explosive formulations using laser electrospray mass spectrometry. *Rapid Commun. Mass Spectrom.* **2010,** *24*, 1659-1664.
(41) Avci, G. F. Y.; Anilanmert, B.; Cengiz, S. Rapid and simple analysis of trace levels of three explosives in soil by liquid chromatography-tandem mass spectrometry. *Acta Chromatogr.* **2017,** *29*, 45-56.
(42) Tian, C.; Yin, J.; Zhao, Z.; Zhang, Y.; Duan, Y. Rapid identification and desorption mechanisms of nitrogen-based explosives by ambient micro-fabricated glow discharge plasma desorption/ionization (MFGDP) mass spectrometry. *Talanta* **2017,** *167*, 75-85.
(43) Tam, M.; Hill, H. H. Secondary electrospray ionization-ion mobility spectrometry for explosive vapor detection. *Anal. Chem.* **2004,** *76*, 2741-2747.
(44) A., J. Y.; A., D. K.; S., N. D.; N., T. A.; K., B. N. Tandem mass spectrometry and density functional theory of RDX fragmentation pathways: role of ion–molecule complexes in loss of NO_3 and lack of molecular ion peak. *Rapid Commun. Mass Spectrom.* **2015,** *29*, 802-810.
(45) Tomás, D.; F., A. J.; M., V. J.; Javier, L. J. Condensed-phase laser ionization time-of-flight mass spectrometry of highly energetic nitro-aromatic compounds. *Rapid Commun. Mass Spectrom.* **2013,** *27*, 1807-1813.
(46) Tang, T. B.; Chaudhri, M. M.; Rees, C. S.; Mullock, S. J. Decomposition of solid explosives by laser irradiation: a mass spectrometric study. *J. Mater. Sci.* **1987,** *22*, 1037-1044.
(47) Mullen, C.; Coggiola, M. J.; Oser, H. Femtosecond laser photoionization time-of-flight mass spectrometry of nitro-aromatic explosives and explosives related compounds. *J. Am. Soc. Mass Spectrom.* **2009,** *20*, 419-429.
(48) Zhang, W.; Shen, R.; Ye, Y.; Wu, L.; Hu, Y.; Zhu, P. Dissociation of cyclotrimethylenetrinitramine under 1064-nm laser irradiation investigated by time-of-flight mass spectrometer. *Spectrosc. Lett.* **2014,** *47*, 611-615.
(49) Zuckermann, H.; Greenblatt, G. D.; Haas, Y. OH formation in the infrared multiphoton decomposition of jet-cooled cyclic nitramines. *J. Phys. Chem.* **1987,** *91*, 5159-5161.
(50) Zhao, X.; Hintsa, E. J.; Lee, Y. T. Infrared multiphoton dissociation of RDX in a molecular beam. *J. Chem. Phys.* **1988,** *88*, 801-810.
(51) Botcher, T. R.; Wight, C. A. Explosive thermal decomposition mechanism of RDX. *J. Chem. Phys.* **1994,** *98*, 5441-5444.
(52) Owens, F. J.; Sharma, J. X-ray photoelectron spectroscopy and paramagnetic resonance evidence for shock-induced intramolecular bond breaking in some energetic solids. *J. Appl. Phys.* **1980,** *51*, 1494-1497.
(53) Patterson, J. E.; Dreger, Z. A.; Miao, M.; Gupta, Y. M. Shock wave induced decomposition of RDX: time-resolved spectroscopy. *J. Phys. Chem. A* **2008,** *112*, 7374-7382.
(54) Miao, M.; Dreger, Z. A.; Patterson, J. E.; Gupta, Y. M. Shock wave induced decomposition of RDX: quantum chemistry calculations. *J. Phys. Chem. A* **2008,** *112*, 7383-7390.
(55) Capellos, C.; Papagiannakopoulos, P.; Liang, Y.-L. The 248 nm photodecomposition of hexahydro-1,3,5-trinitro-1,3,5-triazine. *Chem. Phys. Lett.* **1989,** *164*, 533-538.
(56) Guo, Y. Q.; Greenfield, M.; Bernstein, E. R. Decomposition of nitramine energetic materials in excited electronic states: RDX and HMX. *J. Chem. Phys.* **2005,** *122*, 244310.
(57) Sunku, S.; Gundawar, M. K.; Myakalwar, A. K.; Kiran, P. P.; Tewari, S. P.; Rao, S. V. Femtosecond and nanosecond laser induced breakdown spectroscopic studies of NTO, HMX, and RDX. *Spectrochim. Acta B* **2013,** *79-80*, 31-38.
(58) Postler, J.; Goulart, M. M.; Matias, C.; Mauracher, A.; da Silva, F. F.; Scheier, P.; Limão-Vieira, P.; Denifl, S. Dissociative electron attachment to the nitroamine HMX (octahydro-1,3,5,7-tetranitro-1,3,5,7-tetrazocine). *J. Am. Soc. Mass. Spectrom.* **2013,** *24*, 744-752.
(59) Akin, F. A. Ionisation energy, electron affinity, and mass spectral decomposition mechanisms of RDX isomers upon electron attachment and electron ionisation. *Mol. Phys.* **2016,** *114*, 3556-3566.
(60) Yuan, B.; Bernstein, E. R. Initial mechanisms for the unimolecular decomposition of electronically excited bisfuroxan based energetic materials. *J. Chem. Phys.* **2017,** *146*, 014301.

(61) Boddu, V. M.; Viswanath, D. S.; Ghosh, T. K.; Damavarapu, R. 2,4,6-Triamino-1,3,5-trinitrobenzene (TATB) and TATB-based formulations—A review. *J. Hazard. Mater.* **2010,** *181*, 1-8.
(62) Makashir, P. S.; Kurian, E. M. Spectroscopic and thermal studies on the decomposition of l,3,5-triamino-2,4,6-trinitrobenzene (TATB). *J. Therm. Anal.* **1996,** *46*, 225-236.
(63) Glascoe, E. A.; Zaug, J. M.; Armstrong, M. R.; Crowhurst, J. C.; Grant, C. D.; Fried, L. E. Nanosecond time-resolved and steady-state infrared studies of photoinduced decomposition of TATB at ambient and elevated pressure. *J. Phys. Chem. A* **2009,** *113*, 5881-5887.
(64) Xiong, Y.; Liu, J.; Zhong, F.; Xu, T.; Cheng, K. Identification of the free radical produced in the photolysis of 1,3,5-triamino-2,4,6-trinitrobenzene (TATB). *J. Phys. Chem. A* **2014,** *118*, 6858-6863.
(65) Tiwari, S. C.; Nomura, K.-i.; Kalia, R. K.; Nakano, A.; Vashishta, P. Multiple reaction pathways in shocked 2,4,6-triamino-1,3,5-trinitrobenzene crystal. *J. Phys. Chem. C* **2017,** *121*, 16029-16034.
(66) Wu, C. J.; Fried, L. E. Ring closure mediated by intramolecular hydrogen transfer in the decomposition of a push−pull nitroaromatic: TATB. *J. Phys. Chem. A* **2000,** *104*, 6447-6452.
(67) He, Z.-H.; Chen, J.; Wu, Q. Initial decomposition of condensed-phase 1,3,5-triamino-2,4,6-trinitrobenzene under shock loading. *J. Phys. Chem. C* **2017,** *121*, 8227-8235.
(68) Zhijian, Y.; Jinshan, L.; Bing, H.; Shijun, L.; Zhong, H.; Fude, N. Preparation and properties study of core‐shell CL-20/TATB composites. *Propellants Explos. Pyrotech.* **2014,** *39*, 51-58.
(69) Singh, A.; Kumar, M.; Soni, P.; Singh, M.; Srivastava, A. Mechanical and explosive properties of plastic bonded explosives based on mixture of HMX and TATB. *Def. Sci. J.* **2013,** *63*, 622-629.
(70) Singh, A.; Sharma, T. C.; Kumar, M.; Narang, J. K.; Kishore, P.; Srivastava, A. Thermal decomposition and kinetics of plastic bonded explosives based on mixture of HMX and TATB with polymer matrices. *Defence Technology* **2017,** *13*, 22-32.
(71) Zhixiang, W.; Xiaode, G.; Fei, W.; Ting, Y. Preparation of HMX/TATB composite particles using a mechanochemical approach. *Propellants Explos. Pyrotech.* **2016,** *41*, 327-333.
(72) Xu, H.; Duan, X.; Li, H.; Pei, C. A novel high-energetic and good-sensitive cocrystal composed of CL-20 and TATB by a rapid solvent/non-solvent method. *RSC Adv.* **2015,** *5*, 95764-95770.
(73) Yin, S.; Bernstein, E. R. Properties of iron sulfide, hydrosulfide, and mixed sulfide/hydrosulfide cluster anions through photoelectron spectroscopy and density functional theory calculations. *J. Chem. Phys.* **2016,** *145*, 154302.
(74) Frisch, M. J.; Trucks, G. W.; Schlegel, H. B.; Scuseria, G. E.; Robb, M. A.; Cheeseman, J. R.; Scalmani, G.; Barone, V.; Mennucci, B.; Petersson, G. A., et al. *Gaussian 09, Revision A.02, Gaussian, Inc., Wallingford CT* **2009**.
(75) Becke, A. D. Density-functional thermochemistry. III. The role of exact exchange. *J. Chem. Phys.* **1993,** *98*, 5648-5652.
(76) Becke, A. D. Density-functional exchange-energy approximation with correct asymptotic behavior. *Phys. Rev. A* **1988,** *38*, 3098-3100.
(77) Lee, C.; Yang, W.; Parr, R. G. Development of the Colle-Salvetti correlation-energy formula into a functional of the electron density. *Phys. Rev. B* **1988,** *37*, 785-789.

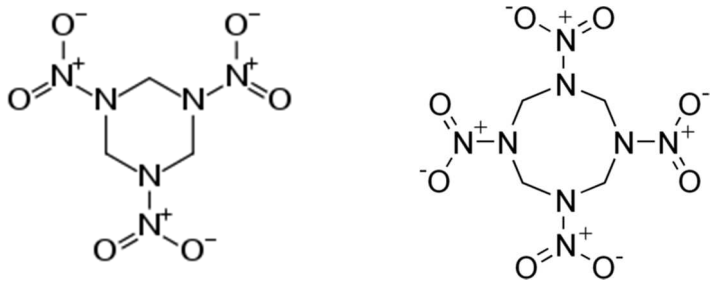

Figure 1 Schematic structures of RDX (left) and HMX (right).

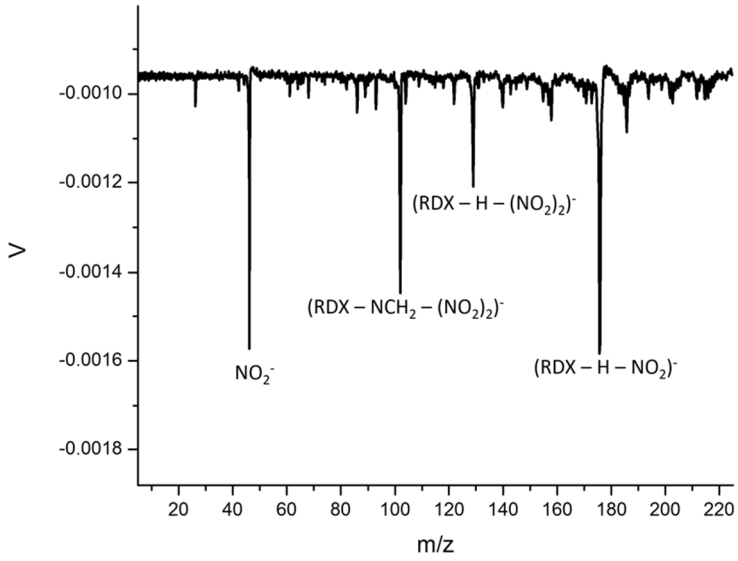

Figure 2 Mass spectrum of RDX sample (RDX/DCM) sprayed on a Zn surface.

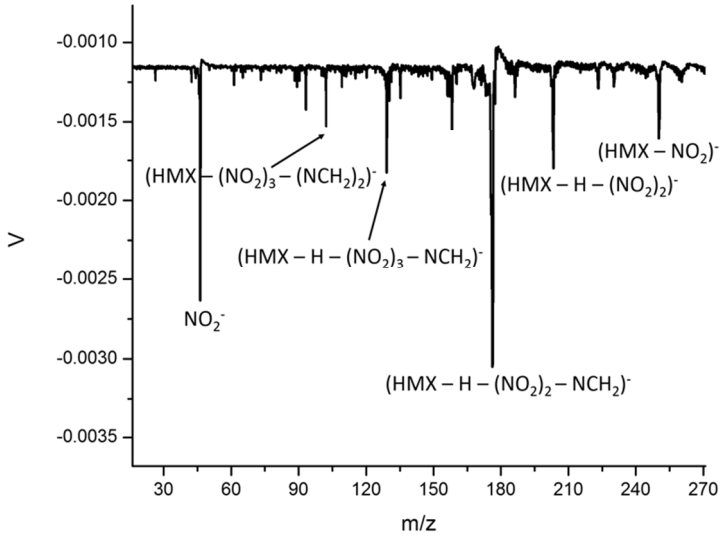

Figure 3 Mass spectrum of HMX sample (HMX/DCM) sprayed on a Zn surface.

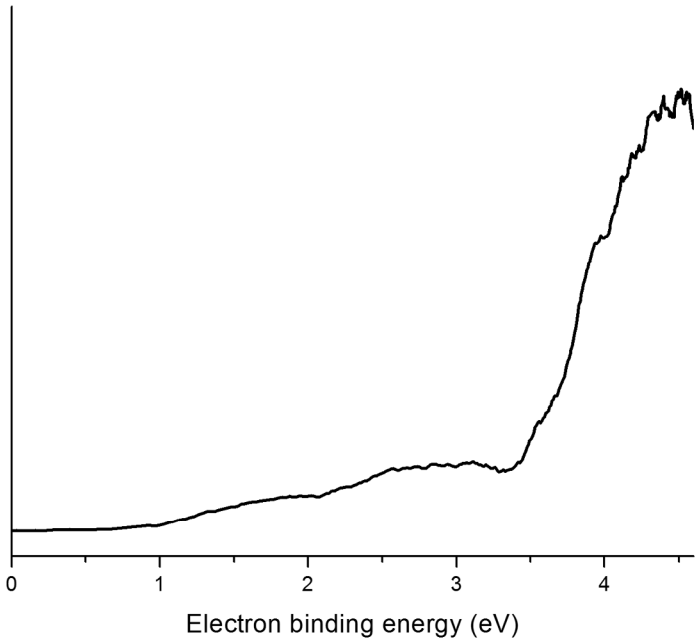

Figure 4 Photoelectron spectra of $(RDX - H - NO_2)^-$ recorded with 266 nm photons. Sample for MALDI is RDX/DCM spayed on a Zn surface.

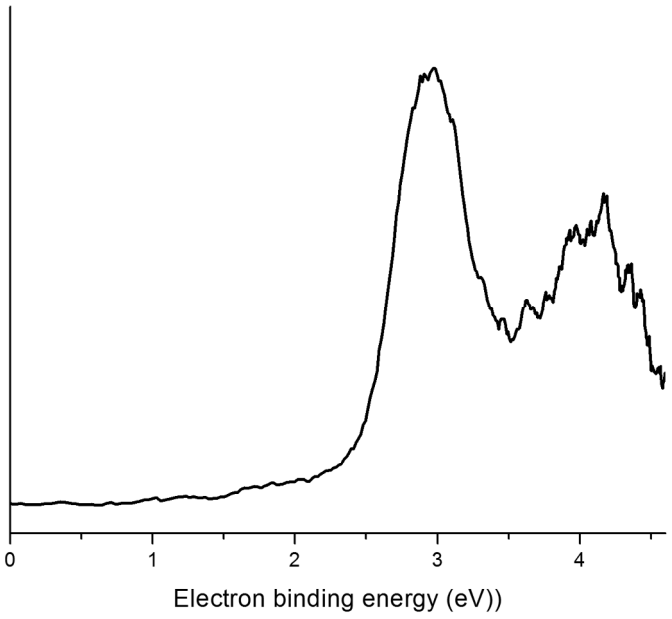

Figure 5 Photoelectron spectra of $(RDX - H - (NO_2)_2)^-$ recorded with 266 nm photons. Sample for MALDI is RDX/DCM spayed on a Zn surface.

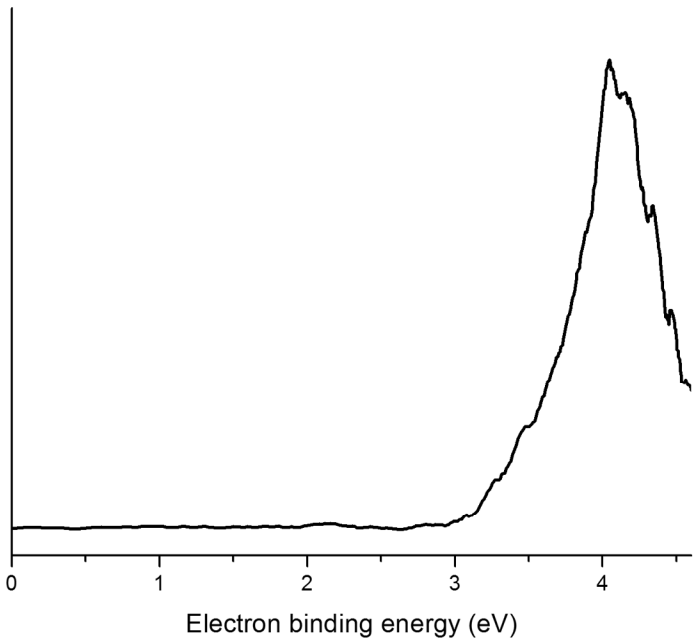

Figure 6 Photoelectron spectra of $(RDX - NCH_2 - (NO_2)_2)^-$ recorded with 266 nm photons. Sample for MALDI is RDX/DCM spayed on a Zn surface.

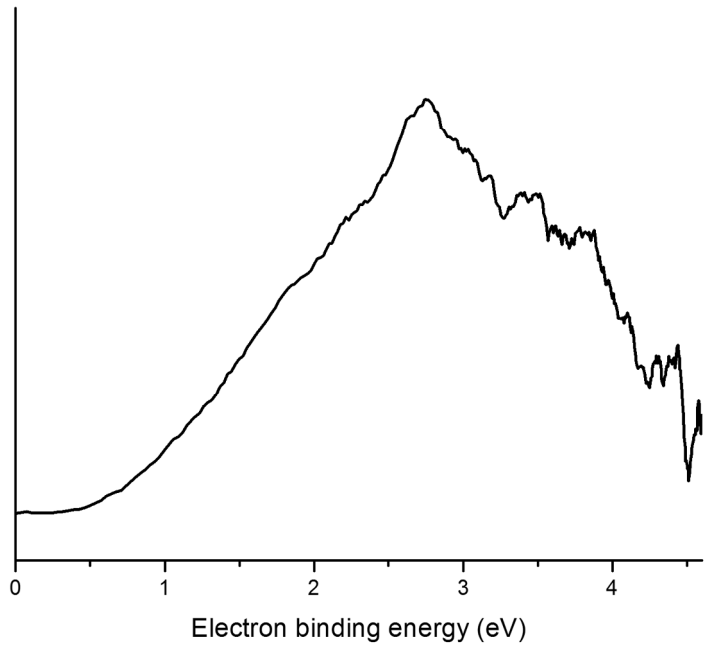

Figure 7 Photoelectron spectra of $(HMX - NO_2)^-$ recorded with 266 nm photons. Sample for MALDI is HMX/DCM spayed on a Zn surface.

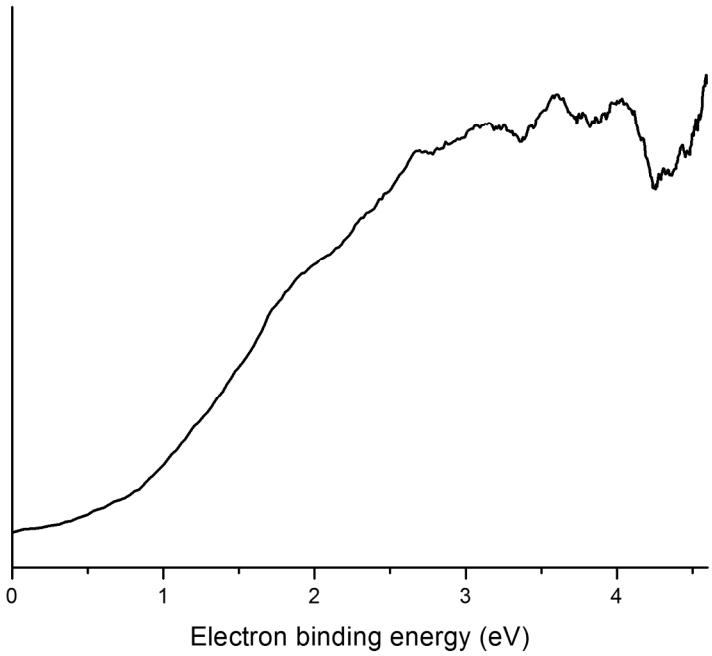

Figure 8 Photoelectron spectra of $(HMX - H - (NO_2)_2)^-$ recorded with 266 nm photons. Sample for MALDI is HMX/DCM spayed on a Zn surface.

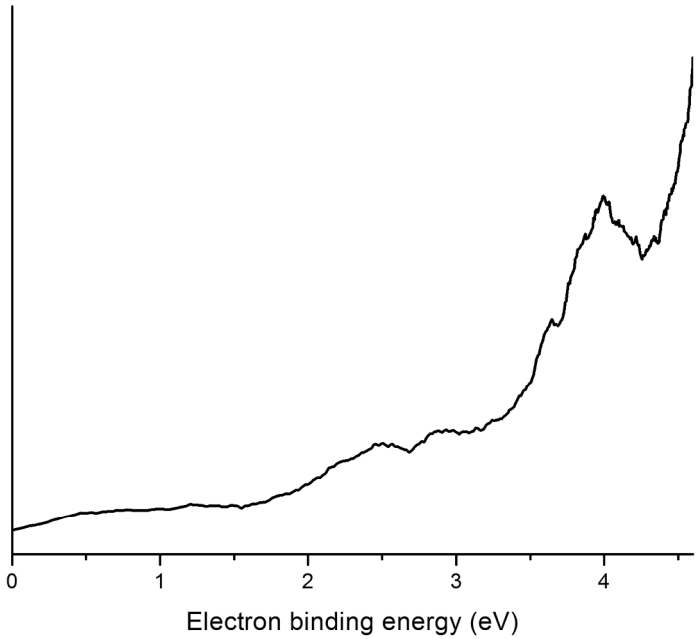

Figure 9 Photoelectron spectra of $(HMX - H - (NO_2)_2 - NCH_2)^-$ recorded with 266 nm photons. Sample for MALDI is HMX/DCM spayed on a Zn surface.

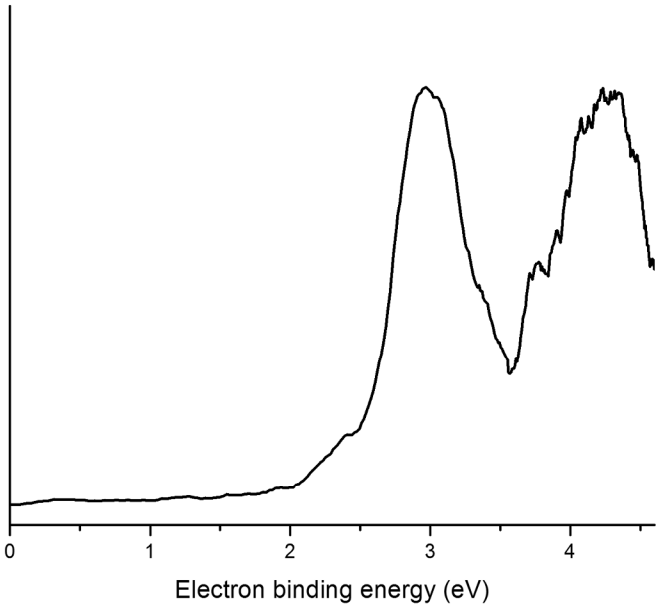

Figure 10 Photoelectron spectra of $(HMX - H - (NO_2)_3 - NCH_2)^-$ recorded with 266 nm photons. Sample for MALDI is HMX/DCM spayed on a Zn surface.

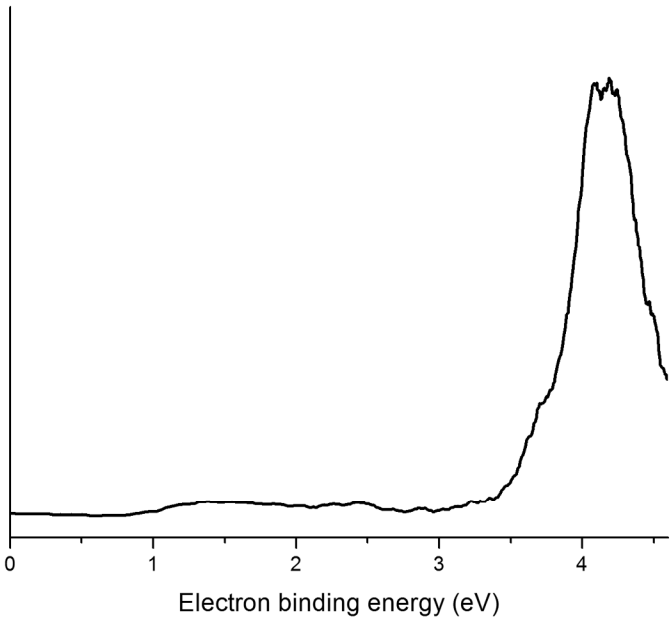

Figure 11 Photoelectron spectra of $(HMX - (NO_2)_3 - (NCH_2)_2)^-$ recorded with 266 nm photons. Sample for MALDI is HMX/DCM spayed on a Zn surface.

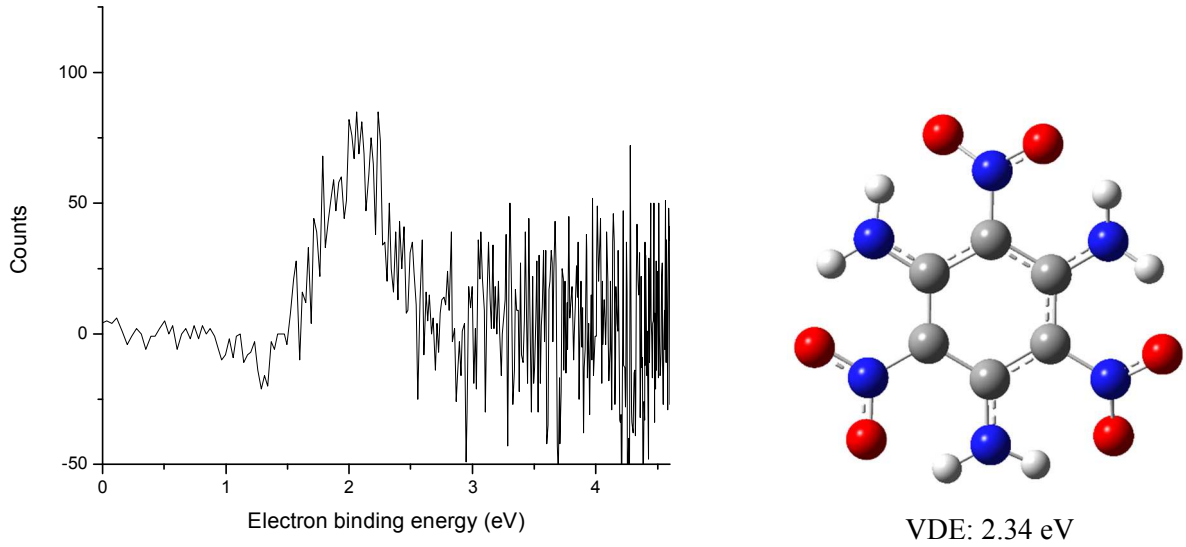

Figure 12 Photoelectron spectra of $TATB^-$ recorded with 266 nm photons with sample (TATB/DCM) spayed on a Zn surface (left) and optimized geometry of $TATB^-$ based on B3LYP/6-311++G(d,p) calculations (right). The calculated VDE is indicated.

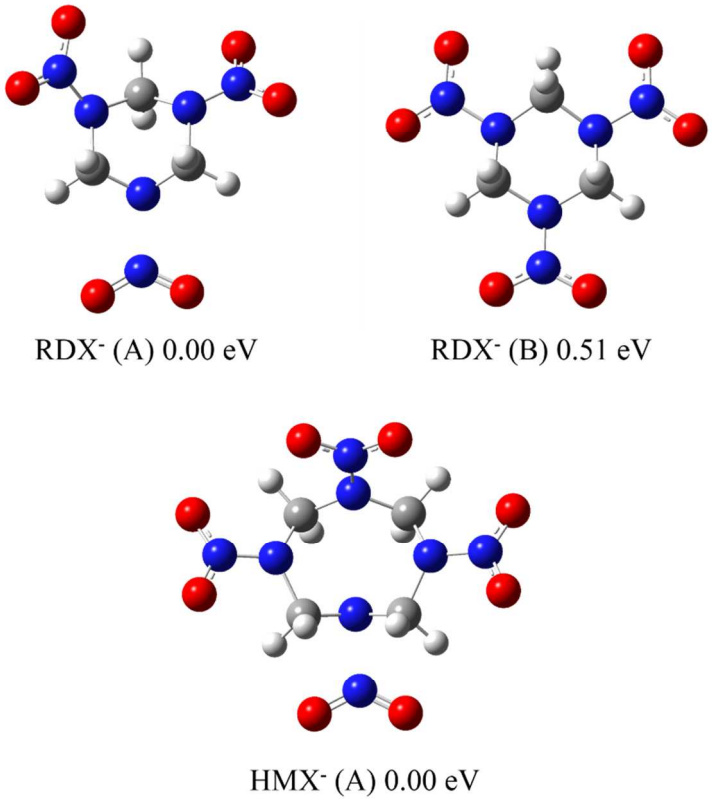

Figure 13 Optimized geometries of the typical low lying anionic isomers of RDX^- and HMX^- based on B3LYP/6-311++G(d,p) calculations. Relative energies are indicated.

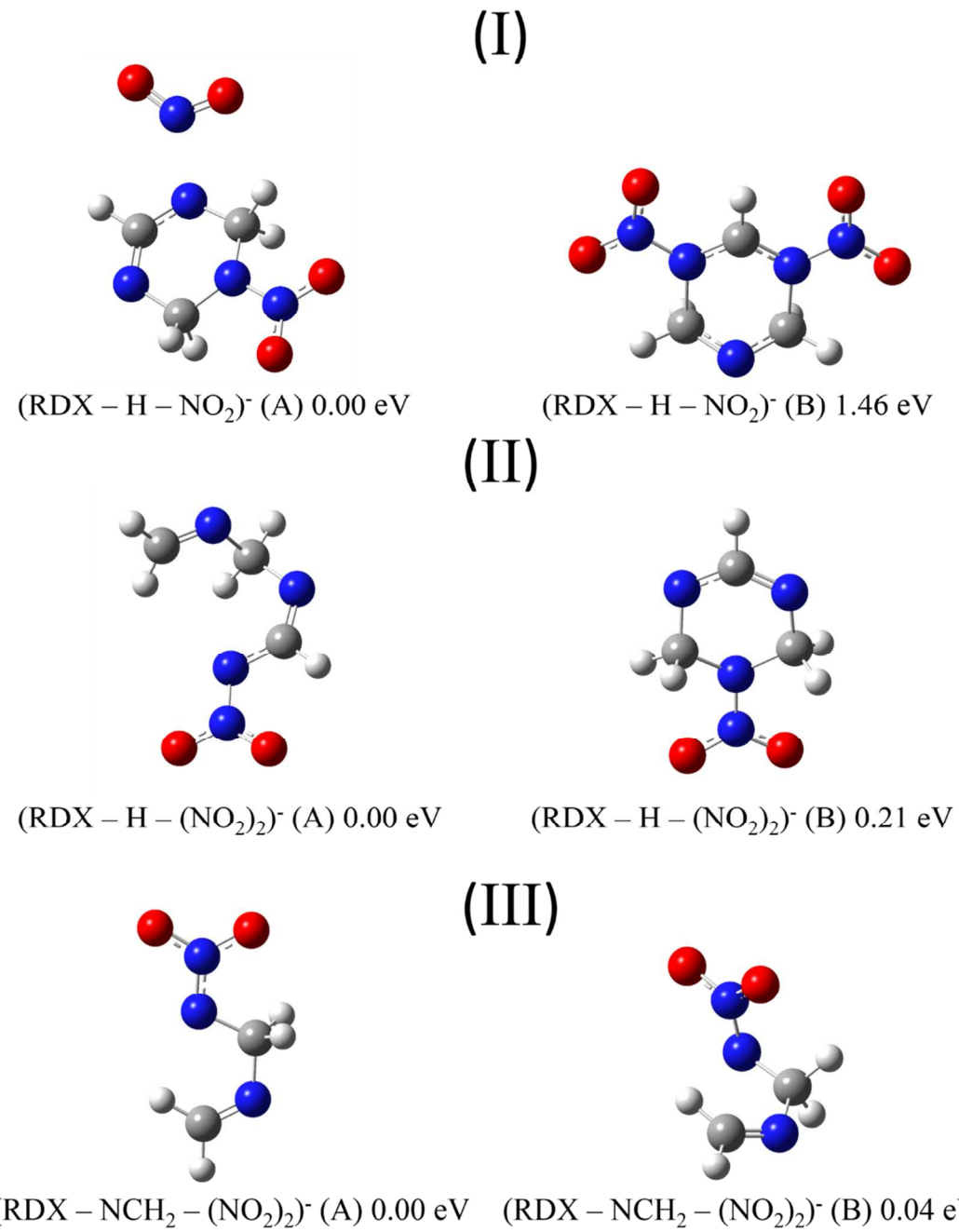

Figure 14 Optimized geometries of the typical low lying anionic isomers of (I) $(RDX – H – NO_2)^-$, (II) $(RDX – H – (NO_2)_2)^-$, and (III) $(RDX – NCH_2 – (NO_2)_2)^-$ based on B3LYP/6-311++G(d,p) calculations. Relative energies are indicated.

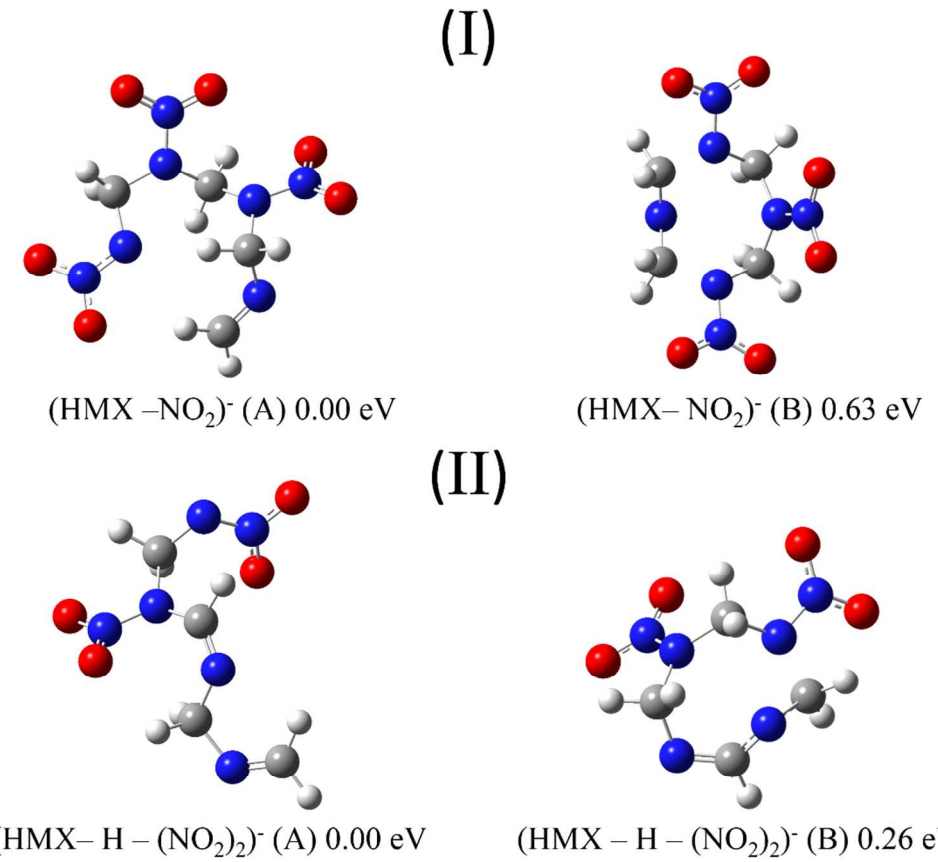

Figure 15 Optimized geometries of the typical low lying anionic isomers of (I) $(HMX - NO_2)^-$, and (II) $(HMX - H - (NO_2)_2)^-$ based on B3LYP/6-311++G(d,p) calculations. Relative energies are indicated.

(I)

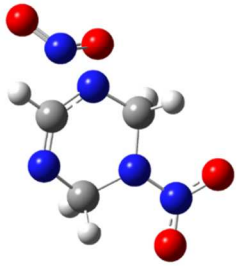

$(HMX - H - (NO_2)_2 - NCH_2)^-$ (A) 0.00 eV

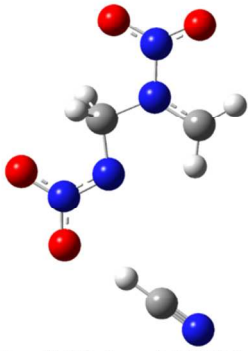

$(HMX - H - (NO_2)_2 - NCH_2)^-$ (B) 0.53 eV

(II)

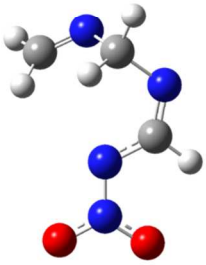

$(HMX - H - (NO_2)_3 - NCH_2)^-$ (A) 0.00 eV

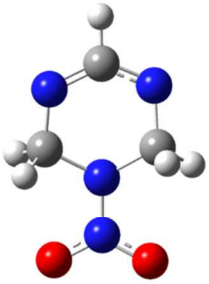

$(HMX - H - (NO_2)_3 - NCH_2)^-$ (B) 0.21 eV

(III)

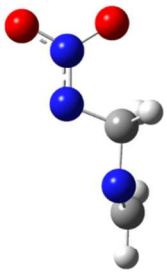

$(HMX - (NO_2)_3 - (NCH_2)_2)^-$ (A) 0.00 eV

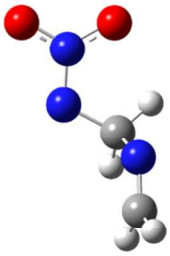

$(HMX - (NO_2)_3 - (NCH_2)_2)^-$ (B) 0.06 eV

Figure 16 Optimized geometries of the typical low lying anionic isomers of (I) $(HMX - H - (NO_2)_2 - NCH_2)^-$, (II) $(HMX - H - (NO_2)_3 - NCH_2)^-$, and (III) $(HMX - (NO_2)_3 - (NCH_2)_2)^-$ based on B3LYP/6-311++G(d,p) calculations. Relative energies are indicated.

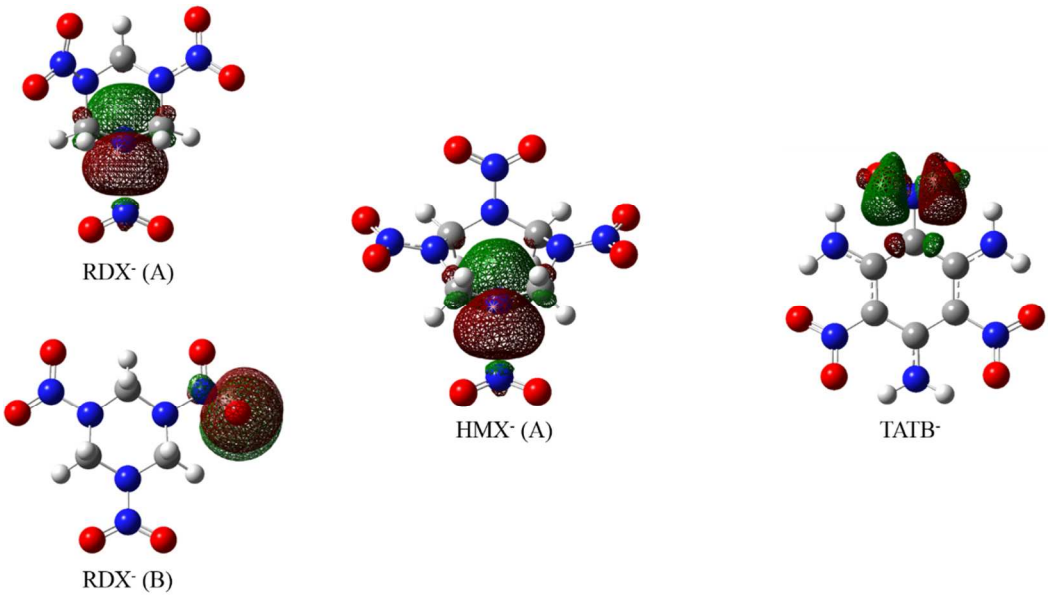

Figure 17 NBO/HOMOs (highest occupied molecular orbitals) of anionic parent species of RDX^-, HMX^-, and $TATB^-$ from an NBO analysis based on B3LYP/6-311++G(d,p) DFT calculations.

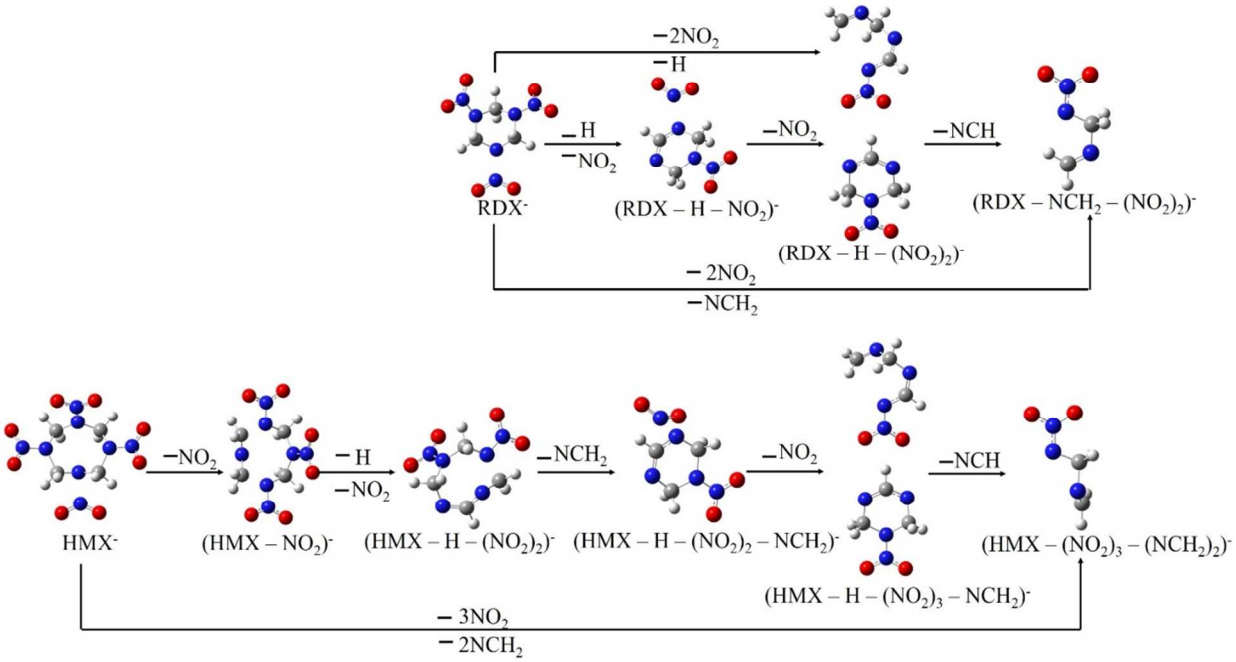

Figure 18 The dissociation pathways of RDX and HMX anions.

Table 1 Relative energies (ΔE) of the low energy isomers of RDX^-, and HMX^- related species, and comparison of their calculated VDEs based on a B3LYP/6-311++G(d,p) algorithm. Experimental measurements are at the right hand column. All energies are in eV.

		B3LYP/6-311++G(d,p)		Exp. VDE
		ΔE	Theo. VDE	
RDX^-	RDX^- (A)	0.00	4.38	—
	RDX^- (B)	0.51	1.77	
$(RDX – H – NO_2)^-$	$(RDX – H – NO_2)^-$ (A)	0.00	4.51	> 4.4
	$(RDX – H – NO_2)^-$ (B)	1.46	2.56	
$(RDX – H – (NO_2)_2)^-$	$(RDX – H – (NO_2)_2)^-$ (A)	0.00	4.27	4.15
	$(RDX – H – (NO_2)_2)^-$ (B)	0.21	2.97	2.97
$(RDX – NCH_2 – (NO_2)_2)^-$	$(RDX – NCH_2 – (NO_2)_2)^-$ (A)	0.00	3.94	4.10
	$(RDX – NCH_2 – (NO_2)_2)^-$ (B)	0.04	3.95	
HMX^-	HMX^- (A)	0.00	2.21	—
$(HMX – NO_2)^-$	$(HMX – NO_2)^-$ (A)	0.00	4.99	
	$(HMX – NO_2)^-$ (B)	0.63	3.93	~2.84
$(HMX – H – (NO_2)_2)^-$	$(HMX – H – (NO_2)_2)^-$ (A)	0.00	4.93	
	$(HMX – H – (NO_2)_2)^-$ (B)	0.26	3.90	> 3.5
$(HMX – H – (NO_2)_2 – NCH_2)^-$	$(HMX – H – (NO_2)_2 – NCH_2)^-$ (A)	0.00	4.22	3.99
	$(HMX – H – (NO_2)_2 – NCH_2)^-$ (B)	0.53	4.34	
$(HMX – H – (NO_2)_3 – NCH_2)^-$	$(HMX – H – (NO_2)_3 – NCH_2)^-$ (A)	0.00	4.27	4.20
	$(HMX – H – (NO_2)_3 – NCH_2)^-$ (B)	0.21	2.98	2.97
$(HMX – (NO_2)_3 – (NCH_2)_2)^-$	$(HMX – (NO_2)_3 – (NCH_2)_2)^-$ (A)	0.00	3.81	4.17
	$(HMX – (NO_2)_3 – (NCH_2)_2)^-$ (B)	0.06	3.82	

TOC Graphic

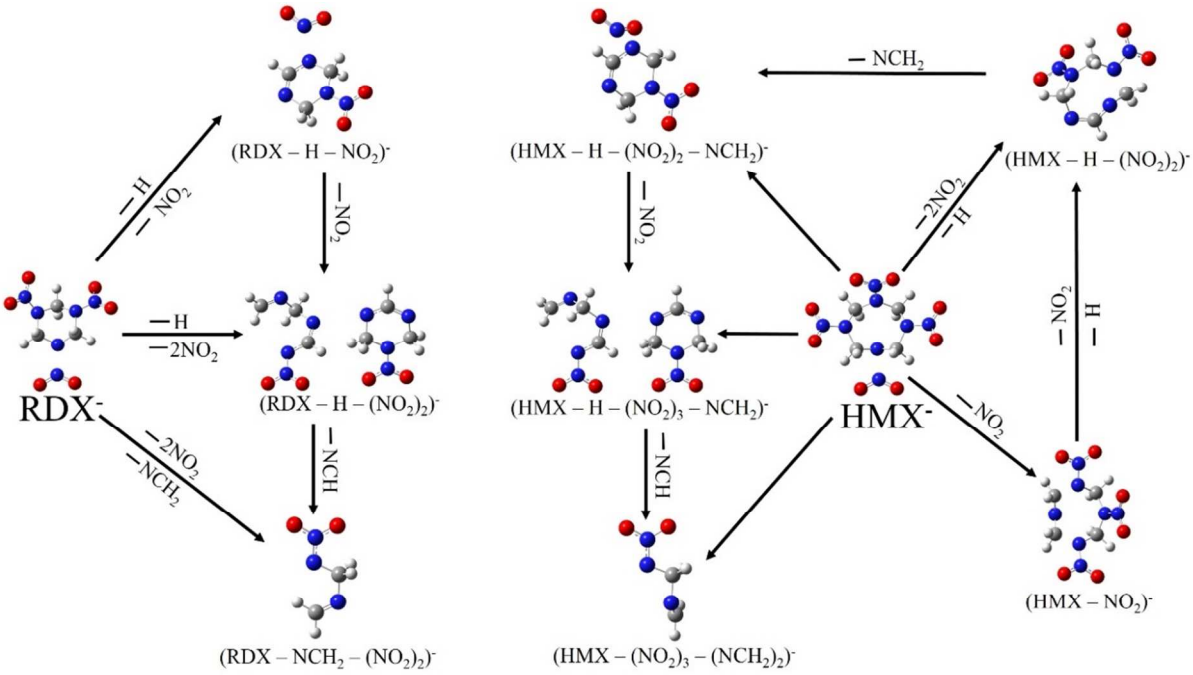
RDX-
(RDX – H – NO2)-
(RDX – H – (NO2)2)-
(RDX – NCH2 – (NO2)2)-
HMX-
(HMX – H – (NO2)2 – NCH2)-
(HMX – H – (NO2)2)-
(HMX – H – (NO2)3 – NCH2)-
(HMX – NO2)-
(HMX – (NO2)3 – (NCH2)2)-
– H
– NO2
– 2NO2
– NCH2
– NCH
– NO
– NCH2